Size is Everything: Universal Features of Quasar Microlensing with Extended Sources

by

Michael J. Mortonson

Submitted to the Department of Physics
in partial fulfillment of the requirements for the degree of

Bachelor of Science in Physics

at the

MASSACHUSETTS INSTITUTE OF TECHNOLOGY

June 2004

Author .....
Department of Physics
May 7, 2004

Certified by .....
Paul L. Schechter
William A. M. Burden Professor of Astrophysics
Thesis Supervisor

Accepted by .....
Professor David E. Pritchard
Senior Thesis Coordinator, Department of Physics

Size is Everything: Universal Features of Quasar Microlensing with Extended Sources

by

Michael J. Mortonson

Submitted to the Department of Physics
on May 7, 2004, in partial fulfillment of the
requirements for the degree of
Bachelor of Science in Physics

Abstract

We examine the effect that the shape of the source brightness profile has on the magnitude fluctuations of images in lens systems due to microlensing. We do this by convolving a variety of accretion disk models (including Gaussian disks, uniform disks, "cones," and a Shakura-Sunyaev thermal model) with two magnification patterns in the source plane, one with convergence $\kappa = 0.4$ and shear $\gamma = 0$ (positive parity), and the other with $\kappa = \gamma = 0.6$ (negative parity). By looking at magnification histograms of the convolutions and using chi-squared tests to determine the number of observations that would be necessary to distinguish histograms associated with different disk models, we find that, for circular disk models, the microlensing fluctuations are relatively insensitive to all properties of the models except the half-light radius of the disk.

Thesis Supervisor: Paul L. Schechter
Title: William A. M. Burden Professor of Astrophysics

Acknowledgments

I owe many thanks to my advisor, Paul Schechter, who introduced me to gravitational lensing, suggested that I investigate the effects of source properties on quasar microlensing, and provided helpful advice and criticism at all stages of my research. I am also grateful to Joachim Wambsganss for some useful discussions and for the magnification patterns that were the starting point for my work, and to Rob Simcoe and Ron Remillard for their help with chi-square tests.

I would like to thank Karyn, my parents, and my friends for their continual support and encouragement. Finally, I give thanks to my fellow classmates in physics for making the work and stress easier to bear.

Contents

List of Figures

List of Tables

Chapter 1

Introduction

Gravitational lensing, the deflection, magnification, and distortion of light from distant sources by intervening mass such as galaxies or stars, is an astronomical tool with many uses, including measuring the dark matter content of galaxies, studying the structure of quasars, and estimating the values of cosmological parameters.

This variety of applications is sometimes a shortcoming, however. When trying to model a specific lens system, for example, we are plagued with an overabundance of parameters to choose from. We know that all these factors should have some sort of effect on what we observe, but we do not always know which factors are the most important and which could be ignored. As a result of having so many parameters, there is a problem of degeneracies in modeling lens systems, where systems with different lens or source properties can produce the same set of images (e.g., Courbin, Saha, & Schechter, 2002). It is important to find out which parameters have little effect on the observables in lensing so that those properties can be neglected in lens models. Including these extra details just adds unnecessary complications to the models and obscures the properties of the lens system that really matter.

In a subfield of gravitational lensing, microlensing, the size of the source can have a large effect on the brightnesses of the images. It is not clear, however, what effect the *shape* of the source has, or if there is any significant effect at all. Here we examine this question by studying the observable changes in microlensing when we vary the distribution of light from the source.

Chapter 2

Gravitational Lensing Basics

From Einstein's theory of general relativity, we know that light is deflected by massive objects. Since gravitational fields curve not only space, but spacetime, massive objects in the vicinity of a photon's path also affect the time that the photon appears to take to travel along that path.

Imagine a photon traveling from some distant source in space to an observer on Earth. In the absence of any mass between the source and the observer, the photon travels in a straight line. If, however, we put a massive object directly between the source and the observer (and imagine that the photon can still travel on a straight path through the object), the photon appears to travel more slowly[1] as it passes through the region where the gravitational potential is strongest, so the shortest path is no longer a straight line. A photon that travels in a wide curve around the mass, however, will also have a time delay, simply because its path is longer than the straight-line path. The optimal path must balance between gravitational increase of travel time and extra path length.

[1] One can view this time delay as if the light were traveling through a medium with a refractive index $n = 1 - 2\Phi$, where Φ is the gravitational potential (Narayan & Bartelmann, 1996).

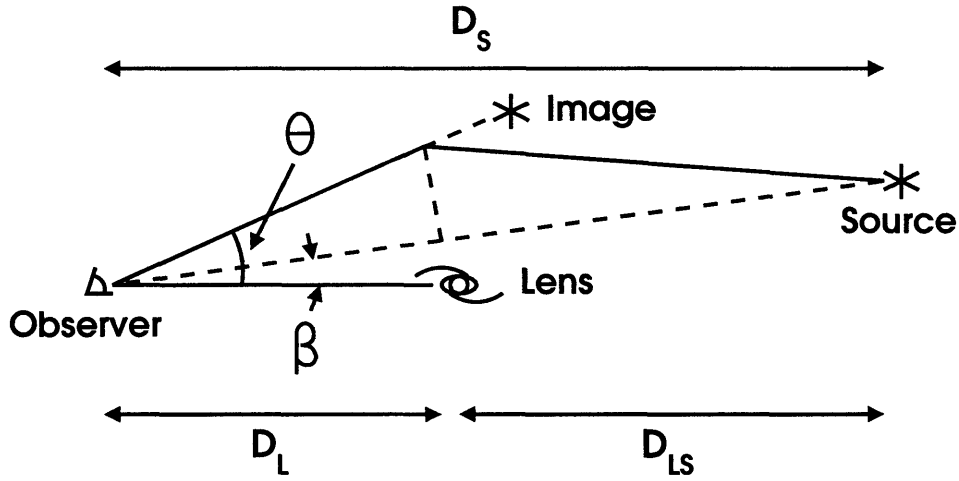

Figure 2-1: Geometry of strong gravitational lensing. Multiple images are possible, and the lens, source, observer, and image positions do not necessarily lie in the same plane. For simplicity, however, only one image is depicted here and the lens geometry is projected into a plane.

2.1 Time-Delay Function and Fermat's Principle

We can construct a time-delay function to express the additional time it takes a photon to travel along some arbitrary path compared to the travel time along a straight-line path in the absence of a gravitational field: $t = t_{geom} + t_{grav}$.

Fermat's principle states that light travels along paths of extremal time, which for lensing means paths for which the time-delay function has a local minimum, saddle point, or maximum (Courbin, Saha, & Schechter, 2002). At each of these points an observer will see an image, so under certain conditions a lens will produce multiple images of a source.

As with scattering in particle physics, virtually all of the photon's deflection occurs in a small region near the lens mass. We can therefore assume that the photon travels along a straight path from the source to the lens, and from the lens to the observer, but with some deflection angle at the lens itself. Then the component of the time-delay function due to extra path length, t_{geom}, can be calculated using simple geometry (see

Figure 2-1). Assuming that $\theta - \beta \ll 1$,

$$t_{geom} = \frac{D_L D_S}{2D_{LS}}(\boldsymbol{\theta} - \boldsymbol{\beta})^2 \tag{2.1}$$

in units where $c = 1$, where $\boldsymbol{\theta}$ and $\boldsymbol{\beta}$ are now vectors in the plane of the sky indicating the angular separations of the image and the source, respectively, from the lens. The distances D_L, D_S, and D_{LS} are all angular diameter distances (Narayan & Bartelmann, 1996).[2]

To find the gravitational contribution to the time-delay function, also known as the Shapiro delay (Shapiro, 1964), we assume that the fields are weak, meaning that the gravitational potential satisfies $|\Phi| \ll 1$. At a distance of a few kiloparsecs from the center of a 10^{12}-$M_\odot$ galaxy modeled by an isothermal sphere with a circular velocity $v_c \approx 300$ km/s, $|\Phi| \sim 10^{-6}$, so this approximation is justified in most cases of interest. We assume that the mass distribution of the lens is static over the time it takes for light to travel across it, so Φ is a function of space but not time. The spacetime metric with a single mass (with potential Φ) localized at the origin is (Carroll, 2004)

$$d\tau^2 = (1 + 2\Phi)dt^2 - (1 - 2\Phi)(dx^2 + dy^2 + dz^2). \tag{2.2}$$

For a photon, $d\tau = 0$, so $dt = (1-2\Phi)dl$ to first order in Φ, where $dl = \sqrt{dx^2 + dy^2 + dz^2}$ is an infinitesimal path length. Integrating along the path of the photon, we find that

$$t_{grav} = -\int 2\Phi dl. \tag{2.3}$$

Assuming that the angle of deflection is small, we can approximate the integral in Equation (2.3) by $-\int 2\Phi dx$, taking x to be the direction along the line of sight. We then define a two-dimensional lensing potential,

$$\psi \equiv \frac{2D_{LS}}{D_L D_S}\int \Phi dx. \tag{2.4}$$

[2]Angular diameter distances are defined such that an object of size l that subtends an angle θ in the sky is at an angular diameter distance $D = l/\theta$.

Using this definition, and including an overall factor of $(1 + z_L)$, where z_L is the lens redshift, to shift into the observer's reference frame, we can write the time-delay function as

$$t(\boldsymbol{\theta}) = (1 + z_L)\frac{D_L D_S}{D_{LS}}\left[\frac{1}{2}(\boldsymbol{\theta} - \boldsymbol{\beta})^2 - \psi(\boldsymbol{\theta})\right]. \tag{2.5}$$

Using Fermat's principle, we can find the locations of the images by solving

$$\boldsymbol{\nabla} t(\boldsymbol{\theta}) = \boldsymbol{\theta} - \boldsymbol{\beta} - \boldsymbol{\nabla}\psi(\boldsymbol{\theta}) = 0. \tag{2.6}$$

2.2 Magnification of Images

Lensing not only affects the positions of images, but also stretches and distorts them. Starting with Equation (2.6) and taking derivatives with respect to θ_i $(i = 1, 2)$, we get the inverse magnification matrix (Narayan & Bartelmann, 1996):

$$M^{-1} = \frac{\partial \boldsymbol{\beta}}{\partial \boldsymbol{\theta}} = \left(\delta_{ij} - \frac{\partial^2 \psi}{\partial\theta_i \partial\theta_j}\right). \tag{2.7}$$

This matrix can be written in terms of the convergence, κ, and the shear, γ, which are related to the lensing potential $\psi(\boldsymbol{\theta})$ by

$$\begin{aligned}
\kappa &\equiv \frac{1}{2}\left(\frac{\partial^2\psi}{\partial\theta_1^2} + \frac{\partial^2\psi}{\partial\theta_2^2}\right), \\
\gamma_1 &\equiv \frac{1}{2}\left(\frac{\partial^2\psi}{\partial\theta_1^2} - \frac{\partial^2\psi}{\partial\theta_2^2}\right) = \gamma\cos(2\phi), \text{ and} \\
\gamma_2 &\equiv \frac{\partial^2\psi}{\partial\theta_1\partial\theta_2} = \gamma\sin(2\phi),
\end{aligned} \tag{2.8}$$

where ϕ is the orientation angle of the shear, and $\gamma_1^2 + \gamma_2^2 = \gamma^2$ (Narayan & Bartelmann, 1996). The convergence is the dimensionless version of the lens surface density, Σ, and the shear measures the anisotropic stretching of the lens in the direction determined by the angle ϕ. Using κ and the components of γ, the inverse magnification matrix becomes

$$M^{-1} = \begin{pmatrix} 1 - \kappa - \gamma_1 & -\gamma_2 \\ -\gamma_2 & 1 - \kappa + \gamma_1 \end{pmatrix}. \tag{2.9a}$$

Diagonalizing this matrix, we get

$$\begin{pmatrix} 1-\kappa-\gamma & 0 \\ 0 & 1-\kappa+\gamma \end{pmatrix}, \tag{2.9b}$$

where the new basis vectors are rotations of the original vectors $\hat{\boldsymbol{\theta}}_1$ and $\hat{\boldsymbol{\theta}}_2$ by the shear orientation angle ϕ. The scalar magnification, the ratio of the image brightness to the source brightness, is equal to the determinant of the magnification matrix:

$$\mu = \det M = \frac{1}{\det M^{-1}} = \frac{1}{(1-\kappa)^2 - \gamma^2}. \tag{2.10}$$

If $\kappa + \gamma > 1$, then the magnification μ is negative. The sign of μ is associated with the parity of the image; the parity of an extended source is reversed in an image that has a negative value of μ.

It is important to note that lensing conserves the surface brightness of the source (brightness per unit solid angle), so images are magnified by covering a larger area (solid angle) than the source. Conservation of surface brightness is a consequence of Liouville's Theorem (Narayan & Bartelmann, 1996).

2.3 Point Mass Lens

One of the simplest lens systems is a lens consisting of a single point mass, with mass M. The two-dimensional potential for a point mass is $\psi(\boldsymbol{\theta}) = k \ln \theta$, where $\theta = |\boldsymbol{\theta}|$ and $k \equiv \frac{4GMD_{LS}}{D_L D_S}$ is a constant (Courbin, Saha, & Schechter, 2002). Using Equation (2.6) gives

$$\boldsymbol{\theta} - \boldsymbol{\beta} = \boldsymbol{\nabla}(k \ln \theta) = \frac{k}{\theta^2}\boldsymbol{\theta}, \tag{2.11}$$

which shows that $\boldsymbol{\beta}$ and $\boldsymbol{\theta}$ have the same or opposite direction. Solving for $\boldsymbol{\theta}$, we get

$$\boldsymbol{\theta} = \frac{1}{2}\left(\beta \pm \sqrt{\beta^2 + 4k}\right)\hat{\boldsymbol{\beta}}, \tag{2.12}$$

where $\beta = |\boldsymbol{\beta}|$ and $\hat{\boldsymbol{\beta}} = \boldsymbol{\beta}/\beta$.

If the source is collinear with the lens and observer ($\beta = 0$), Equation (2.12) becomes $\theta = \sqrt{k}$. Since there is no preferred direction away from the lens, the image forms a circular ring around the lens with an angular radius of

$$\theta_E = \sqrt{\frac{4GMD_{LS}}{D_L D_S}}. \tag{2.13}$$

This type of image is called an Einstein ring, and θ_E is called the Einstein radius. Even in systems with different kinds of lenses and different geometries, θ_E is a characteristic scale for the image separations (Courbin, Saha, & Schechter, 2002). In the source plane, the Einstein radius is

$$r_E = \theta_E D_S = \sqrt{\frac{4GMD_{LS}D_S}{D_L}}. \tag{2.14}$$

For $\beta = 0$, any circular mass distribution for the lens will form an Einstein ring if the mass is compact enough to fit within its own Einstein radius (Courbin, Saha, & Schechter, 2002). This happens at a critical density, Σ_C. If we consider a uniform sheet of mass, then $\pi\theta_E^2\Sigma_C = M$, so

$$\Sigma_C = \frac{1}{4\pi G}\frac{D_L D_S}{D_{LS}}, \tag{2.15}$$

where Σ_C has units of mass per solid angle.

Using the critical density, we can write a second formula for the convergence. By combining the first line of Equation (2.8) and the definition of ψ in Equation (2.4), we find

$$\kappa = \frac{1}{2}\nabla^2\psi = \frac{D_L D_{LS}}{D_S}\int \nabla^2\Phi dx. \tag{2.16}$$

Now we use Poisson's equation for the potential Φ:

$$\nabla^2\Phi = 4\pi G\rho, \tag{2.17}$$

where ρ is the mass density of the lens. The surface mass density of the lens in the plane of the sky (in units of mass per solid angle) is $\Sigma = D_L^2 \int \rho dx$, so we can write

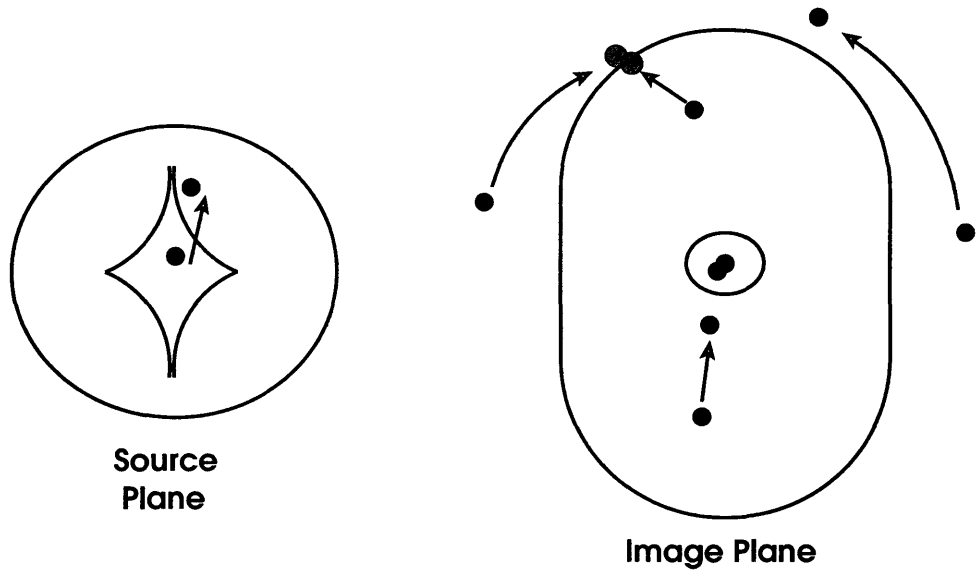

Figure 2-2: An example of caustics and critical lines for an elliptical lens, showing a caustic crossing. As the source (the dot in the source plane) crosses the inner diamond-shaped caustic, two of the images in the image plane (shaded gray) merge and disappear on the outer critical line. Based on figures in Courbin, Saha, & Schechter (2002).

Equation (2.16) as

$$\kappa = \frac{\Sigma}{\Sigma_C}. \tag{2.18}$$

2.4 Critical Lines and Caustics

For lenses more complicated than the point mass or other simple circularly symmetric distributions, keeping track of the images becomes much more difficult. It is useful to introduce two sets of curves: critical lines in the image plane and caustics in the source plane (Courbin, Saha, & Schechter, 2002). These curves map on to each other, so that when the source is on a caustic, an image appears on a critical line. Pairs of images merge and then disappear, or appear and then split apart, at critical lines, with one image on each side of the line. Images near a critical line are also extremely bright. Since the critical lines are where images are created or destroyed, the caustics form boundaries such that when the source crosses a caustic, the total number of

images changes by two. An example for the case of an elliptical lens is shown in Figure 2-2.

Chapter 3

Observations

The deflection of light by massive objects was proposed by Newton, predicted by Einstein's general relativity, and confirmed experimentally by Eddington's observation of the deflection of starlight by the sun in 1919 (Dyson, Eddington, & Davidson, 1920). Throughout the 1920s and 1930s, it was known that not only could light be deflected by a gravitational field, but it could also be separated into multiple images by gravity (Eddington, 1920; Chwolson, 1924; Einstein, 1936). However, most people at the time thought that actually observing such an effect was out of the question. This changed when Zwicky (1937a) predicted that galaxies could produce observable splitting of light from distant sources, and that there should be significant numbers of lens systems within reach of observers (Zwicky, 1937b). It was over 40 years before the first lens was discovered by Walsh et al. (1979): Q0957+561, a pair of images of a quasar at a redshift of $z = 1.41$. The first quadruple lens detected was PG1115+080 (Weymann et al., 1980).

In the late 1980s, lensed radio quasars were discovered, some of which had complete or partial Einstein rings (Hewitt et al., 1987). Extended images in the forms of arcs or arclets, galaxies lensed by foreground galaxy clusters, were also observed (Soucail et al., 1987a,b; Lynds & Petrosian, 1986; Tyson, 1988; Fort et al., 1998; Tyson, Valdes, & Wenk, 1990).

Many lenses of various types have been discovered over the past few decades. A partial list is presented in Courbin, Saha, & Schechter (2002). A catalog of several

more observed lens systems can be found at the website for CASTLES, the CfA-Arizona Space Telescope Lens Survey (Kochanek et al., 2004).

Through studies of gravitational lenses, we can learn about both the sources, which are magnified by lenses, and the lensing masses (often galaxies), whose properties affect the image positions and relative fluxes. We can also use lensing to constrain cosmological parameters. Refsdal (1964) suggested that differences in time delays between images in a lens system could be used to place limits on the Hubble constant, H_0. Surveys that look for faint gravitational signatures of large-scale structure through weak lensing and statistical modeling of lenses also aim to constrain parameters such as the matter density of the universe and the amount of vacuum energy.

Observers measuring time delays look for correlated variations in the brightnesses of different images (Courbin, Saha, & Schechter, 2002). Intrinsic variability of the sources produces these kinds of fluctuations. Uncorrelated brightness variations have also been observed, for instance in Q0957+561 (Falco, Wambsganss, & Schneider, 1991) and the "Einstein cross" or "Huchra's Lens," Q2237+0305 (Ostensen et al., 1996). One possible reason for these uncorrelated fluctuations is microlensing, which is due to stars in the lensing galaxy and produces images separated by microarcseconds, too close to be resolved (Courbin, Saha, & Schechter, 2002). Microlensing of quasars will be discussed in more detail in the next chapter. Microlensing has also been used for searches for dark matter (in the form of MACHOs) in the galactic halo, an idea suggested by Paczyński (1986b) and carried out by several groups (Alcock et al., 1993; Aubourg et al., 1993; Udalski et al., 1993; Alard, 1995).

Chapter 4

Quasar Microlensing

The smooth potentials used to model lensing galaxies are only approximations. The stars that make up the galaxies have their own potentials, which, when added together, introduce "lumpiness" to the overall galaxy potential. This produces small bumps and valleys in the surface of the time-delay function, leading to the production of more images.

The separations of these additional images should be on the order of the Einstein radii of the lensing stars. For a one-solar mass object at a distance of 10 Gpc, $\theta_E \approx$ 1 μarcsec. This is far too small an angle to be resolved by any present-day instruments, but changes in the magnitudes of these microimages can affect the brightness of the entire bundle of microimages (the "macroimage"). If the source is smaller than the Einstein radii of the microlenses, then relative motion between the source, the field of lensing stars, and the observer will cause the macroimage's magnitude to fluctuate. Since light from different macroimages in a lens system passes through different parts of the lensing galaxy, the fluctuations in the resolved images are uncorrelated with each other.

Since there is no way to know the exact positions and velocities of the stars that act as microlenses in a particular galaxy, we approximate the system as a field of stars randomly distributed in a plane. With so many objects and parameters, few analytical results can be obtained for quasar microlensing. Instead, numerical simulations are used to model microlensing and make predictions.

One technique for studying quasar microlensing numerically is the method of ray-shooting (Courbin, Saha, & Schechter, 2002; Kayser, Refsdal, & Stabell, 1986; Schneider & Weiss, 1987; Wambsganss, 1990; Wambsganss, Paczyński, & Katz, 1990; Wambsganss, Schneider, & Paczyński, 1990). Since surface area is conserved by lensing, a region in the source plane where the source would be highly magnified corresponds to a large area of light-ray endpoints at the observer. The ray-shooting method turns this around and simulates sending the light rays back from the observer to the source plane. Firing a large number of rays from the observer at random angles leads to a build-up of rays at high-magnification areas of the source plane, while low-magnification regions will be struck by rays less often. The result is a pattern of caustics in the source plane, where the value of the distribution at each point is proportional to the magnification that a source at that position would have (Courbin, Saha, & Schechter, 2002). Simulated microlensing light curves can be produced from these magnification patterns by tracing a path across a pattern and reading off the value at each point along the path. Figure 4-1 shows an example of a magnification pattern produced by the ray-shooting method.

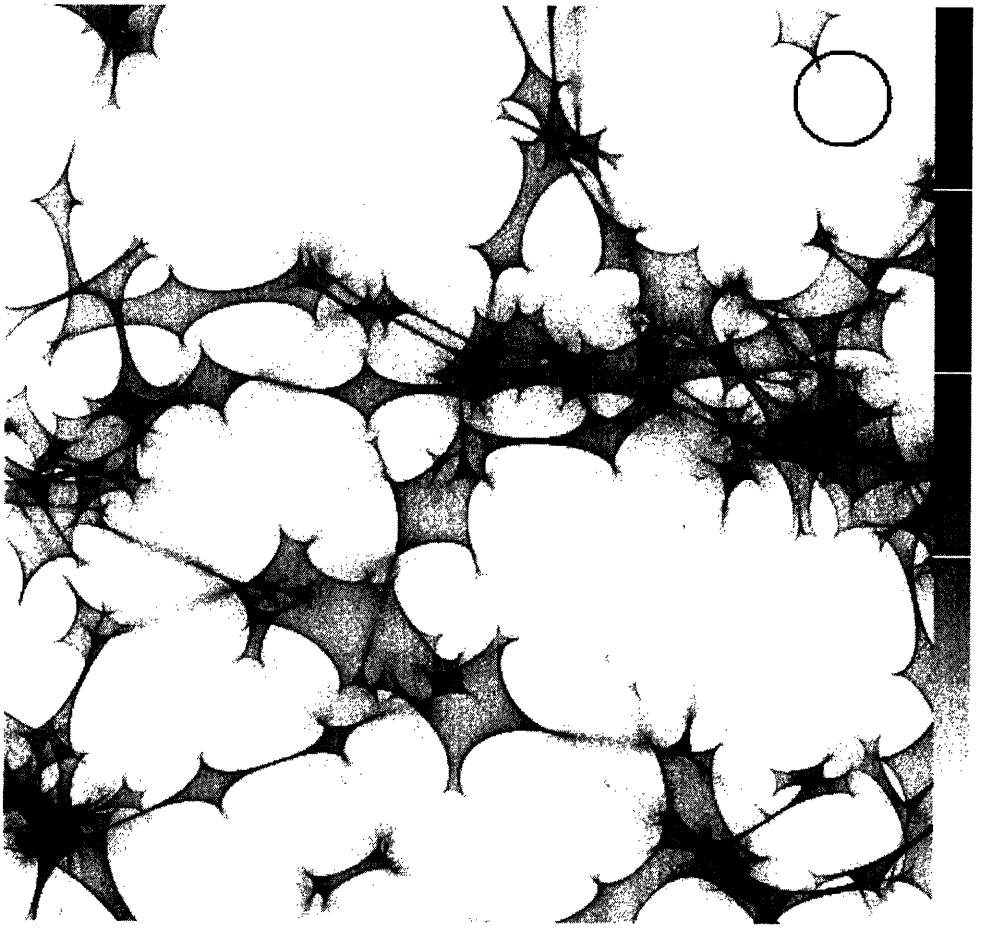

Figure 4-1: A magnification pattern of caustics in the source plane for a positive parity macroimage at a position with convergence $\kappa = 0.4$ and shear $\gamma = 0$. Each side has a length of 20 (microlens) Einstein radii, and the circle in the upper right corner has a radius equal to one Einstein radius. The white lines on the greyscale bar correspond to magnifications that are 1, 2, 3, and 4 times the average macroimage magnification. Dark regions have greater magnification than light regions. 6931 microlenses were used in this simulation, which was provided by Joachim Wambsganss.

Chapter 5

Flux Ratio Anomalies

One of the uses of quasar microlensing is to try to help explain the problem of flux ratio anomalies. These anomalies are observed flux ratios between images in a lens system that disagree with theoretical predictions (Schechter, 2003). One common type of flux ratio anomaly concerns close pairs of images in quadruple lens systems. A theorem states that two images that are close together in a quadruple system should have the same brightness (Gaudi & Petters, 2002). Several systems, including PG1115+080 (Vanderriest et al., 1986; Kristian et al., 1993; Courbin et al., 1997; Iwamuro et al., 2000), MG0414+0534 (Schechter & Moore, 1993), HS0810+2554 (Reimers et al., 2002), and SDSS0924+0219 (Inada et al., 2003) have close pairs that do not obey this theorem, with anomalous flux ratios as high as 10 (Schechter, 2003).

Microlensing has been put forward as one solution to this problem (Schechter, 2003). The theorem mentioned above assumes that the gravitational potential is smooth in the region where light from the close pair of images passes through. As explained in the previous chapter, not only is this assumption incorrect when the lens is a galaxy with billions and billions of stars, but also relaxing this assumption can have a significant effect on the magnitudes of images, and thus on the flux ratios between images.

Microlensing, however, is not the only possible solution. It has also been suggested that the mini-halos that form around galaxies in cold dark matter simulations (Moore et al., 1999) could act as lenses (e.g., Metcalf et al., 2003). Since these mini-halos

are larger than stars but smaller than galaxies, the image separations they would produce are between the scales of strong lensing and microlensing, on the order of milliarcseconds, still too small an angle to resolve separate images (Schechter, 2003).

There are several ways to determine to what extent microlensing and lensing by galactic substructures contribute to explanations of flux ratio anomalies. The fact that mini-halos deflect light by much larger angles than stars do means that sources that are larger than stellar Einstein radii but smaller than mini-halo Einstein radii would be affected by mini-halo lensing but not by microlensing. For example, it is thought that radio quasars emit from regions that fall in this size range, so radio flux ratio anomalies are more likely to be due to mini-halo lensing. Similarly, the size of broad emission line regions is probably between the stellar and mini-halo Einstein radii, whereas continuum emission comes from parts that are smaller than the stellar Einstein radius, so if anomalies are observed in the continuum but not in emission lines, that would point to microlensing (Schechter, 2003).

The time scale for brightness variations caused by mini-halo lensing is on the order of thousands of years, much longer than the microlensing time scale, which is on the order of months or years. Therefore, we can say that the observed uncorrelated variations in the lenses mentioned in Chapter 3 are due to microlensing. Flux ratio anomalies that persist unchanged for a long time, on the other hand, could be the result of mini-halo lensing (Schechter, 2003).

Of course, microlensing and mini-halo lensing do not exhaust the possibilities. While both effects are likely to contribute to flux ratio anomalies at some level, there may be other contributing effects, such as different kinds of halo substructure (Mao et al., 2004; Keeton, Gaudi, & Petters, 2003). In a few cases, it is even possible that the "anomalous" flux ratios can actually be modeled with a smooth potential (Evans & Witt, 2003).

Chapter 6

Factors that Affect Microlensing

6.1 Cosmology

Observations of lensing can be used to study cosmology in a number of ways. The use of time delays to measure the current value of the Hubble constant, as mentioned in Chapter 3, has been carried out with several lens systems (e.g., Koopmans et al., 2003; Kochanek & Schechter, 2004). One of the more recent applications of lensing to cosmology is an effort to predict and observe the effects of weak lensing by large scale structures by measuring the polarization of the cosmic microwave background (e.g., Seljak & Hirata, 2004). Statistical modeling and observations of lensing by galaxy clusters provide possible ways to place constraints on the matter density of the universe (Ω_m) and the dark energy equation of state (e.g., Chae, 2003; Lopes & Miller, 2004; Wambsganss, Bode, & Ostriker, 2004).

Microlensing has more limited applicability to cosmology than other types of gravitational lensing. Some statistical studies of microlensing have been used to place upper limits on the value of Ω_m (Narayan & Bartelmann, 1996), but these constraints are looser than bounds determined by other means.

6.2 The Lens

Perhaps the most obvious factor that can affect microlensing is the mass distribution that makes up the lens. For quasars lensed by foreground galaxies, the microlensing fluctuations depend on the fraction of matter in the galaxy in compact objects, such as stars, and the fraction in smooth dark matter (Schechter & Wambsganss, 2002). Microlensing is also sensitive to substructure in the lensing galaxy (Metcalf et al., 2003). The effect of varying the masses of the microlenses has been studied (Refsdal & Stabell, 1993), and recently, Schechter, Wambsganss, & Lewis (2004) found that the mass function of stars in the lensing galaxy can influence microlensing variability.

There have also been studies of microlensing in the Milky Way Galaxy. Microlensing of sources in the Magellanic Clouds by lenses in the Galactic halo can provide estimates of the contributions of Massive Astrophysical Compact Halo Objects (MACHOs) to the halo (Alcock et al., 1993; Aubourg et al., 1993; Udalski et al., 1992; Alard, 1995; Narayan & Bartelmann, 1996).

Another suggested use of microlensing is to search for extrasolar planets orbiting lensing stars by looking for sharp peaks in the microlensing light curves (Mao & Paczyński, 1991; Gould & Loeb, 1992). Bond et al. (2004) claim to have detected a planet of about 1.5 Jupiter masses around a Galactic halo star using microlensing observations.

6.3 The Source

The size of the source has a large effect on the fluctuations due to microlensing, and this fact has been used to place constraints on the sizes of quasars using observations of extragalactic microlensing (e.g., Wyithe, Webster, & Turner, 2000; Yonehara, 2001; Shalyapin et al., 2002; Wyithe, Agol, & Fluke, 2002; Schechter et al., 2003). "Size" in this context does not necessarily refer only to the size of the quasar as a whole, but also to the sizes of regions of the quasar that emit different kinds of light that can be distinguished observationally. A large extended source covers more microlensing

caustics in the source plane at a single time than a small source, so its brightness varies less as it moves relative to the lens and observer. As a general rule, the variability of a lensed source will only be significantly affected by microlensing if the source is smaller than the projection of the Einstein radius of a microlens into the source plane (Courbin, Saha, & Schechter, 2002).

A related effect could be responsible for differences between emission-line and continuum flux ratios, which have been found in a number of lens systems (e.g., Wisotzki et al., 1993; Schechter et al., 1998; Burud et al., 2002; Wisotzki et al., 2003; Metcalf et al., 2003; Chartas et al., 2004). A possible explanation for these differences is that the broad emission line regions of quasars are larger than the Einstein radii of the microlenses, and the continuum-emitting regions are smaller than the Einstein radii (Moustakas & Metcalf, 2003).

The dependence of temperature on radius in quasar accretion disks leads to another related effect. Since the disk is cooler far from the center than it is near the central black hole, the disk will have a larger effective radius when observed at long wavelengths than it will when observed at short wavelengths. At long wavelengths, therefore, we expect the magnitude variations due to microlensing to be suppressed. The Shakura-Sunyaev accretion disk model (Section 7.4) incorporates the temperature profile of the disk so that we can study the effects on microlensing fluctuations of varying wavelength and source size. Besides using photometric observations of microlensing, it has also been suggested that astrometric observations, looking for small shifts in image positions due to microlensing, could constrain the sizes of quasars at different wavelengths (Lewis & Ibata, 1998; Treyer & Wambsganss, 2004).

It is clear that source size is an important property for quasar microlensing. Depending on how the size of the source is measured, it is possible to imagine sources that have the same size but differ in other ways. For example, if we describe the size of a source by its half-light radius ($r_{1/2}$), the radius at which half of the light is interior to the radius and half of it is outside, then we can construct different source models with the same half-light radii but with their brightness distributed in the source plane in different ways. The brightness of one source may fall off with distance

from the center like a Gaussian, while another could have the same brightness out to a certain radius beyond which there is no light, but these sources could still have equal half-light radii and therefore be the same "size." We will refer to this distribution of brightness as the "shape" of the brightness profile.[1] The question we would like to address is this: for sources with the same size, as determined by the half-light radius, to what extent does the shape of each source influence the fluctuations due to microlensing of the source? The answer to this question tells us how important the shape of the source brightness profile is to observations and models of microlensing.

Agol & Krolik (1999) and Wyithe et al. (2000) have also looked at the connection between source properties and microlensing, but their studies use a large number of parameters for the disk models and focus on light curves and caustic-crossing events. Our models have fewer parameters while still covering a wide range of disk shapes, and our main tool for analyzing the effect on microlensing fluctuations is the magnification histogram.

[1]Note that all of the source models we consider (except in Appendix A) are circularly symmetric, so "shape" does not refer to the shape of the contours of constant brightness, but rather how the spacing of those contours varies with radius.

Chapter 7

Accretion Disk Models

To study the effects of the shape of a source brightness profile on microlensing fluctuations, we use a variety of highly idealized accretion disk models with different shapes to model the source quasar. The first three models (Sections 7.1 to 7.3) are adopted not because they are necessarily realistic, but because they are mathematically simple and span a wide range of possibilities. The fourth model (Section 7.4), while still an idealization, is physically motivated.

7.1 Gaussian Disks

One common type of accretion disk model is a circular two-dimensional Gaussian (e.g., Wyithe, Agol, & Fluke, 2002). The brightness profile can be written

$$G(r) = \frac{L}{2\pi\sigma^2} e^{-r^2/2\sigma^2}, \tag{7.1}$$

where L is the total disk luminosity (with units of erg/s), r is the radius from the center of the disk and σ is the width of the Gaussian.

7.2 Uniform Disks

Although even less realistic than the Gaussian disk, a uniform disk is essentially the simplest disk model imaginable. The uniform disk model has a value of $L/(\pi R^2)$ for radii $0 < r < R$ (where L is the total disk luminosity), and is zero for $r > R$.

7.3 Cones

The "cone" disk model is peaked at the center, and decreases linearly with increasing radius until it reaches zero at a radius R, outside of which the model is zero everywhere. The brightness profile is

$$C(r) = \frac{3L}{\pi R^2}\left(1 - \frac{r}{R}\right), \; r < R, \tag{7.2}$$

where L is the total disk luminosity, r is the radius from the center, and the factor of $3/(\pi R^2)$ is for normalization.

7.4 Shakura-Sunyaev Disks

The last circular accretion disk model we consider is a thin static disk, viewed face-on, with a two-dimensional brightness profile determined by the temperature at each part of the disk. Though more complicated than the previous models, it is still simpler than the similar thermal disk models used by Agol & Krolik (1999) and Wyithe et al. (2000). Many of the results we present in Chapter 9 use this disk model.

We begin with a temperature-radius relation for the disk from Shakura & Sunyaev (1973):

$$T(r) = 2.049 T_0 \left(\frac{r_{in}}{r}\right)^{3/4} \left(1 - \sqrt{\frac{r_{in}}{r}}\right)^{1/4}, \tag{7.3}$$

where T_0 is the peak disk temperature, and r_{in} is the radius of the inner edge of the accretion disk, which we take to be the radius of the innermost stable circular orbit around the central Schwarzschild black hole. Thus, r_{in} depends on the black hole

mass.

We assume that the disk radiates as a black body with an energy density per unit wavelength $u(\lambda, T)$ that depends on the temperature, and therefore on the radius.[1] Using Equation (7.3), we can write the distribution as a function of wavelength and radius:

$$u(\lambda, r)d\lambda = \frac{8\pi hc}{\lambda^5}\left\{\exp\left[0.488\frac{hc}{\lambda kT_0}\left(\frac{r}{r_{in}}\right)^{3/4}\left(1-\sqrt{\frac{r_{in}}{r}}\right)^{-1/4}\right]-1\right\}^{-1}d\lambda. \quad (7.4)$$

It is convenient to use dimensionless variables for the parameters, so we define a dimensionless wavelength, x, and a dimensionless radius, s:

$$x \equiv \frac{kT_0}{hc}\lambda, \; s \equiv \frac{r}{r_{in}}, \quad (7.5)$$

which makes the black body distribution

$$u(x, s)dx = \frac{a}{x^5}\left\{\exp\left[\frac{0.488}{x}\left(\frac{s^3}{1-s^{-1/2}}\right)^{1/4}\right]-1\right\}^{-1}dx, \quad (7.6)$$

where we define $a \equiv 8\pi r_{in}^2 hc\left(\frac{kT_0}{hc}\right)^4$. For the maximum disk temperature T_0 (at $r = 1.36r_{in}$), the peak of $u(x, s)$ is at $x_0 = 0.2014$.

Since the disk radiates at cooler temperatures with increasing distance from the center, observations at different wavelengths will detect different parts of the disk (Wambsganss & Paczyński, 1991; Gould & Miralda-Escudé, 1997). To take the wavelength dependence into account, we define a set of filters associated with specific ranges of the dimensionless wavelength x. The filters are numbered in the direction of increasing wavelength, with filter 0 centered at $x = x_0$. The ranges of x are chosen so that the filters span the space of wavelengths without overlapping (that is, $x_{i,max} = x_{i+1,min}$ where $x_{i,min}$ and $x_{i,max}$ are the minimum and maximum wavelengths for filter i). We assume that each filter transmits 100% of the light in its wavelength

[1] All wavelengths are assumed to be in the quasar frame, so to compare with wavelengths in the observer's frame the quasar's redshift must be accounted for.

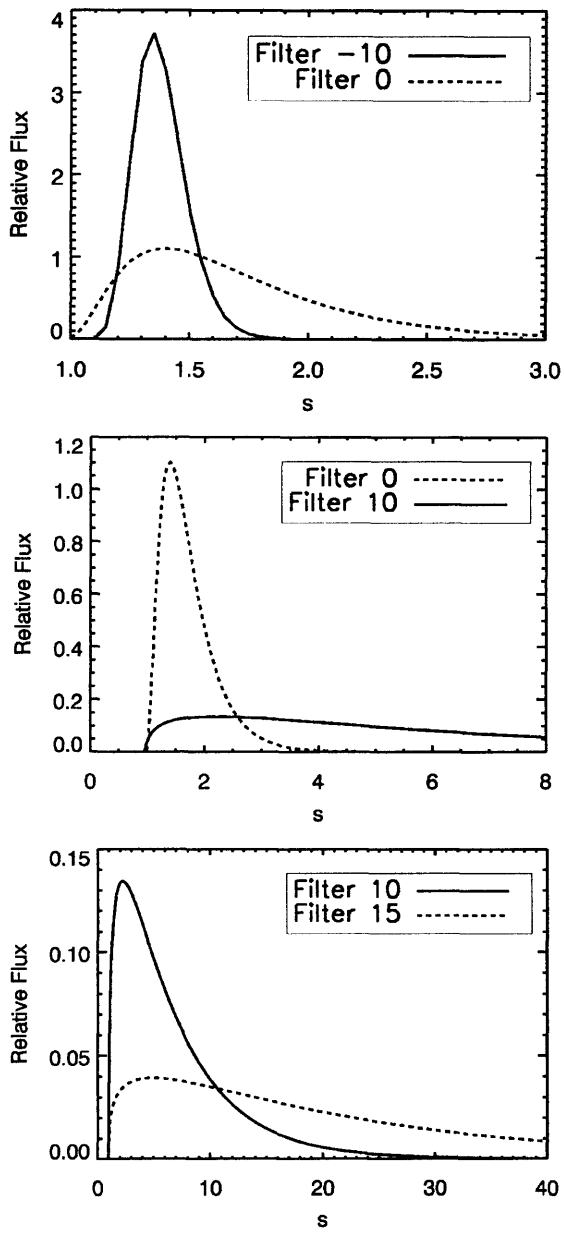

Figure 7-1: Radial intensity distributions ($2\pi sI(s)$) for an $r_{in} = 0.2r_E$ Shakura-Sunyaev disk model in four filters, with central wavelengths $x_{-10} = 0.0271$, $x_0 = 0.2014$, $x_{10} = 1.498$, and $x_{15} = 4.086$. The vertical axis is normalized so that the total disk intensity equals unity.

range. The filters have constant $\Delta(\log x) = \frac{\Delta x}{x_i} = \frac{1}{5}$, so

$$x_i \approx e^{0.2i-1.6025}, \tag{7.7}$$

where x_i is the central wavelength of filter i.

To create a model of the disk as it would be seen through a particular filter i, we integrate the black body distribution over the wavelengths included in the filter:[2]

$$u_i(s) = \int_{x_{i,min}}^{x_{i,max}} u(x,s)dx. \tag{7.8}$$

Then we can define

$$L_i \equiv 2\pi \int_1^\infty \frac{c}{4} u_i(s)sds, \tag{7.9}$$

the total luminosity of the disk in filter i. If we change variables from s back to r for comparison with the Gaussian disk, uniform disk, and cone models, and define

$$f_i(r) \equiv \frac{cu_i(s(r))}{4L_i}, \tag{7.10}$$

then the flux from the disk in filter i is

$$F_i(r) = \frac{L_i}{r_{in}^2} f_i(r), \tag{7.11}$$

which has the same form as Equations (7.1) and (7.2). Radial brightness profiles in four filters are shown in Figure 7-1.

The Shakura-Sunyaev disk model that we end up with depends on two parameters: r_{in}, the innermost radius of the disk, and i, the filter number. The temperature T_0 only determines the relation between λ and x.

[2]For narrow filters, the wavelength across a single filter can be treated as a constant, x_i, as in Kochanek (2004). This eliminates the need to do the integral in Equation (7.8), since $u_i(s) \approx u(x_i, s)$. Note, however, that in Kochanek (2004), the factor of $(1 - \sqrt{r_{in}/r})^{1/4}$ in Equation (7.3) is neglected, so those disk models differ significantly from ours for $r \sim r_{in}$.

7.5 Other Models

Our Shakura-Sunyaev disk model is similar to the thin accretion disk models used by Agol & Krolik (1999) and Jaroszyński, Wambsganss, & Paczyński (1992). Those models are more complicated, however, as they include rotating black holes, tilted disks, and relativistic effects. (See Appendix A about elliptical Gaussian disk models, which can be used to approximate tilted disks.) Microlensing simulations with nonthermal models have also been considered (Rauch & Blandford, 1991), but we do not include such models in this study.

Chapter 8

Magnification Patterns

The effect of microlenses on the total macroimage flux may be represented by a pattern of caustics in the source plane, where the value at each point of the pattern is equal to the magnification of the source at that point, relative to the average macroimage magnification (Kayser, Refsdal, & Stabell, 1986; Paczyński, 1986a; Wambsganss, 1990; Wambsganss, Schneider, & Paczyński, 1990). The microlensing light curve of a point source can be found by tracing a path across the magnification pattern (e.g., Paczyński, 1986a; Wambsganss, Schneider, & Paczyński, 1990; Kochanek, 2004). For an extended source, we must first convolve the source profile with the magnification pattern to find the magnification due to microlensing at each location in the source plane (e.g., Wyithe, Agol, & Fluke, 2002).

The patterns, which were kindly provided by Joachim Wambsganss, were made using ray-shooting techniques that simulate sending rays from the observer through the lens to the source plane, as described in Chapter 4 (Kayser, Refsdal, & Stabell, 1986; Schneider & Weiss, 1987; Wambsganss, 1990; Wambsganss, Paczyński, & Katz, 1990; Wambsganss, Schneider, & Paczyński, 1990). The patterns are 2000 by 2000 pixel arrays with sides of length 100 Einstein radii. We examined two cases: a positive parity image (minimum of the time-delay function) with convergence $\kappa = 0.4$ (all in compact objects), shear $\gamma = 0$, and theoretical average magnification $\mu = 2.778$; and a negative parity image (saddle point) with $\kappa = 0.6$ (again, all in compact objects), $\gamma = 0.6$, and $\mu = -5$. Magnification patterns for each case are shown in

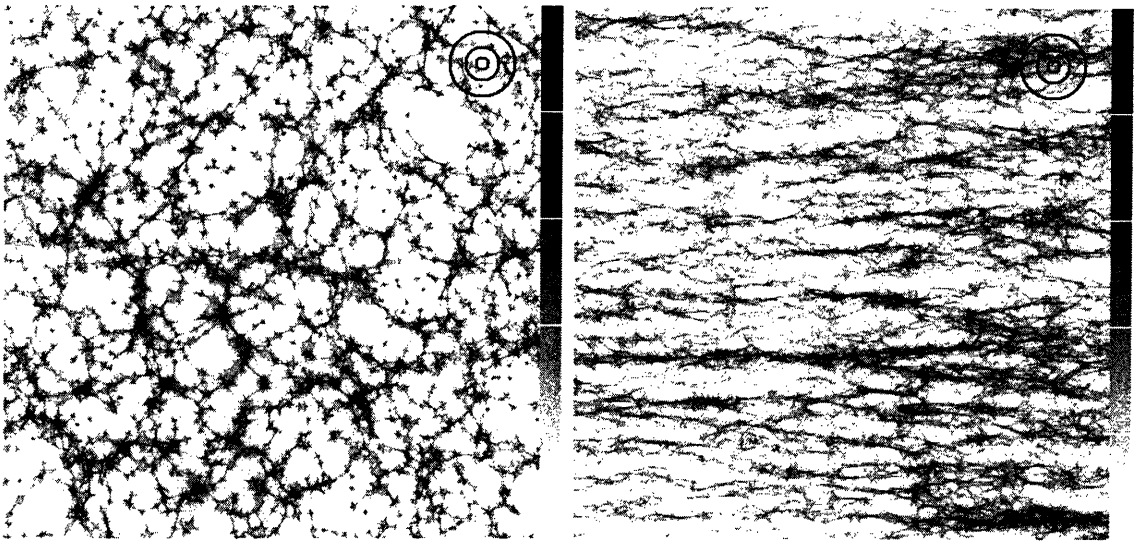

Figure 8-1: Magnification patterns in the source plane for a positive parity image with $\kappa = 0.4$, $\gamma = 0$ (left) and a negative parity image with $\kappa = \gamma = 0.6$ (right). The length of each side is 100 Einstein radii. The white lines on the greyscale bar correspond to magnifications that are 1, 2, 3, and 4 times the average macroimage magnification. Dark regions have greater magnification than light regions. The black circles have radii of 1, 3, and 6 Einstein radii for comparison with the accretion disk models.

Figure 8-1. The positive parity simulation included 8011 lenses, and the negative parity simulation included 56,224 lenses.

For each disk model we wished to study, we used the relevant equation from Chapter 7 to create a 2000 by 2000 pixel array for the disk brightness profile, A. Let us call the original magnification pattern M. By the convolution theorem, we can convolve M and A by multiplying their two-dimensional Fourier transforms and then taking the inverse Fourier transform of the product. This produces a new 2000 by 2000 pixel magnification pattern,

$$C = \mathrm{fft}^{-1}\left[\mathrm{fft}(M)\mathrm{fft}(A)\right], \tag{8.1}$$

where fft and fft^{-1} stand for the fast Fourier transform and the inverse fast Fourier transform, respectively (e.g., Press et al., 1992). Figure 8-2 shows two examples of magnification patterns from convolutions with Shakura-Sunyaev disk models. Sample

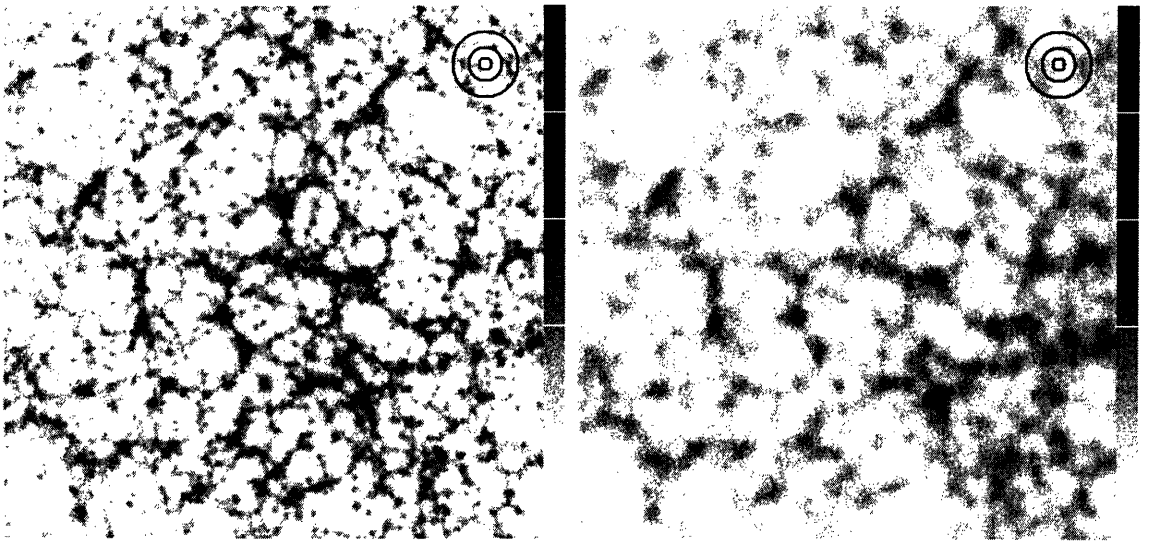

Figure 8-2: Examples of magnification patterns from convolving Shakura-Sunyaev disk profiles with the original positive parity pattern in Figure 8-1. The innermost radius of each disk is $r_{in} = 0.2r_E$. For the left pattern, the filter is $i = 0$ with central wavelength x_0, the wavelength of the peak of the blackbody distribution at the maximum temperature T_0; the disk intensity peaks around $r = 1.4r_{in}$ at this wavelength. For the right pattern the filter is $i = 10$ with central wavelength $x_{10} = 7.44x_0$, and the peak of the disk intensity is approximately at $r = 2.2r_{in}$. The scale and the reference circles are the same as in Figure 8-1.

light curves for paths through these patterns are shown in Figure 8-3.

The longest wavelengths used in our simulations were chosen so that at least 95% of the accretion disk intensity would lie within the 2000 by 2000 pixel area of the magnification pattern. At longer wavelengths, the cooler temperatures of the disk at large radii make the outer regions of the disk more important than in the shorter-wavelength filters. If we use too long a wavelength, a large fraction of the disk intensity spills out of the area of our simulation, making the results inaccurate. The wavelength at which this occurs varies with r_{in}. Although the cutoff is 95%, for the majority of filters used the fraction of light included in the 2000 by 2000 pixel area is above 99%.

At the short-wavelength end, the cutoff was more arbitrary since the disk profiles and their magnification histograms do not vary much with wavelength beyond a certain point that depends on the value of r_{in}. We chose to use wavelengths short

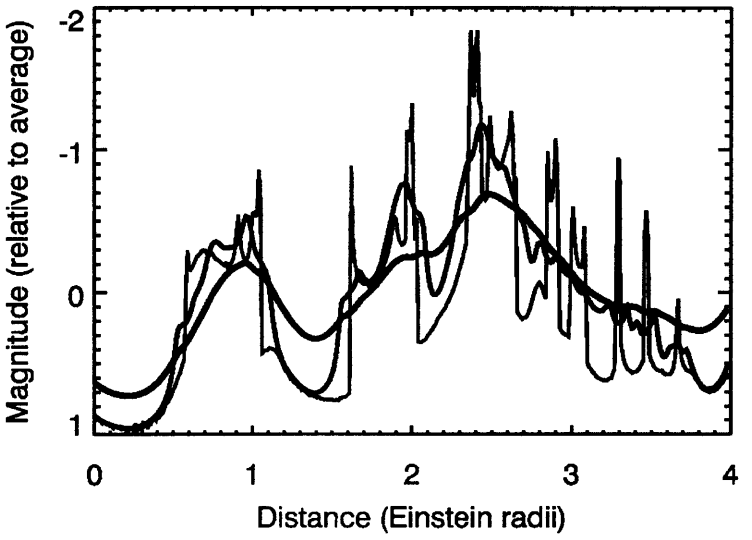

Figure 8-3: Sample light curves from the magnification pattern on the left in Figure 8-1 and both patterns in Figure 8-2 ($\kappa = 0.4$, $\gamma = 0$). The source travels on a vertical path of length 4 Einstein radii in the center of each pattern. The thin curve is from the unconvolved positive parity pattern, the medium curve is from the convolution with the disk viewed in the filter associated with the peak intensity at the maximum temperature T_0 ($i = 0$), and the thick curve is from the convolution in the filter that is a factor of 7.44 longer in wavelength ($i = 10$).

enough to probe values of the half-light radius (see Section 9.2) close to the inner radius r_{in} (within one Einstein radius).

Chapter 9

Magnification Histograms

9.1 Histograms of Convolutions with Shakura-Sunyaev Disks

The values in a magnification pattern are ratios of the macroimage's flux when the source is at a particular point in the pattern, $F(\mathbf{r})$, to the average macroimage flux, $\bar{F} = \mu F_s$, where F_s is the unlensed source intensity. We convert these ratios to magnitude differences,

$$\Delta m = -2.5 \log_{10} \left(\frac{F(\mathbf{r})}{\bar{F}} \right) \tag{9.1}$$

and plot a histogram of Δm for the convolution with each disk model, as in Wambsganss (1992). The number of pixels that fall into each bin of Δm is represented as a probability for the macroimage to have a certain magnitude shift by dividing the number of pixels in the bin by the total number of pixels. Histograms of the original magnification patterns are shown in Figure 9-1.

We made magnification patterns for convolutions with Shakura-Sunyaev disks in several filters with $r_{in} = 0.2r_E$, $0.5r_E$, r_E, and $3r_E$. Some histograms from these patterns are shown in Figures 9-2 and 9-3.

For long wavelengths or large r_{in}, the histograms are sharply peaked at the average macroimage magnification, and there is little difference between the positive and negative parity cases. For small disks at short wavelengths, a low-magnification bump

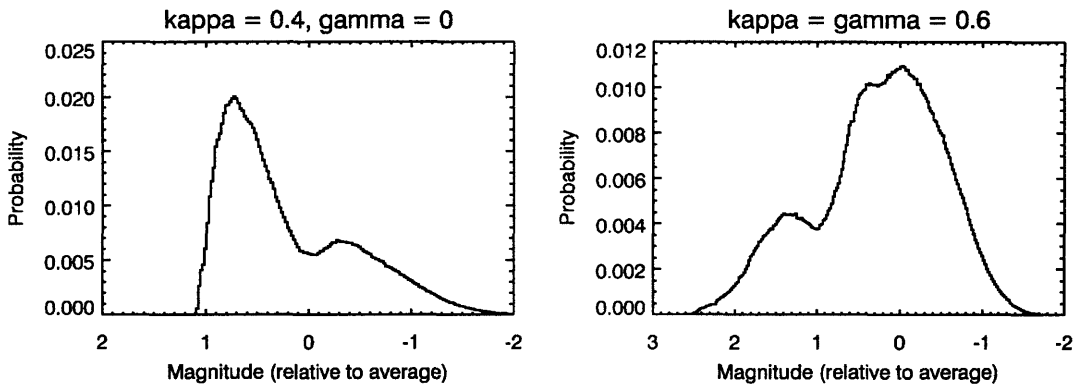

Figure 9-1: Magnification histograms for the unconvolved magnification patterns in Figure 8-1. The left histogram is for the positive parity image, the right, negative parity.

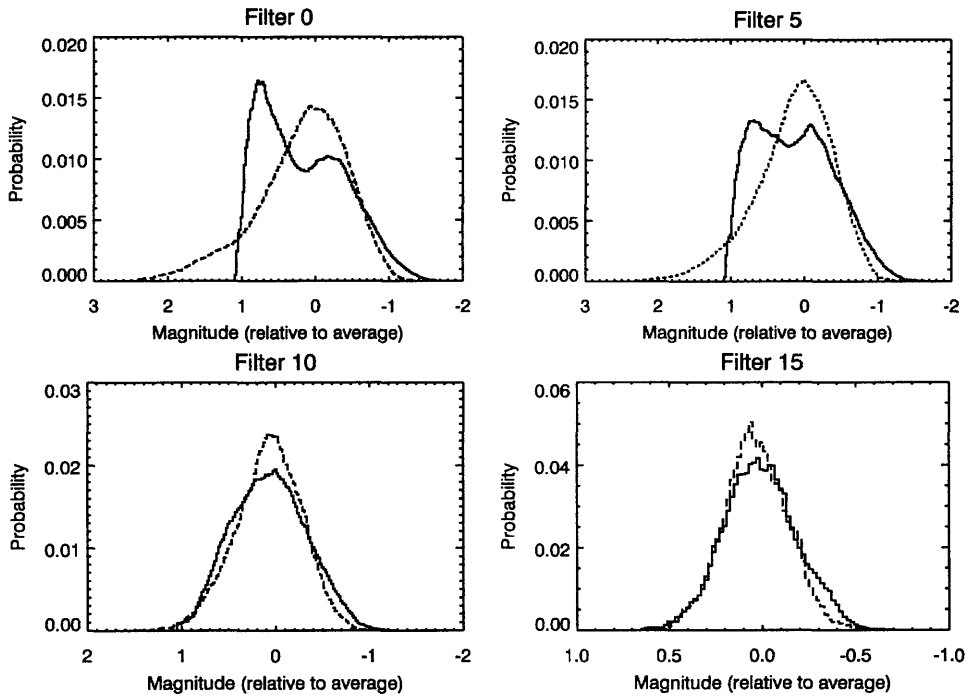

Figure 9-2: Histograms of magnitudes (relative to the magnitude that corresponds to the average macroimage flux) for convolutions of Shakura-Sunyaev disk profiles with $r_{in} = 0.2r_E$ in various filters with the positive parity $\kappa = 0.4$, $\gamma = 0$ magnification pattern (solid curves) and the negative parity $\kappa = \gamma = 0.6$ magnification pattern (dashed curves). The half-light radii of the disks used as sources are $0.28r_E$, $0.41r_E$, $1.00r_E$, and $3.32r_E$, respectively. The histograms at shorter wavelengths than that of the filter associated with the peak intensity at the maximum temperature T_0 (upper left) are all very similar, and so they are not shown here.

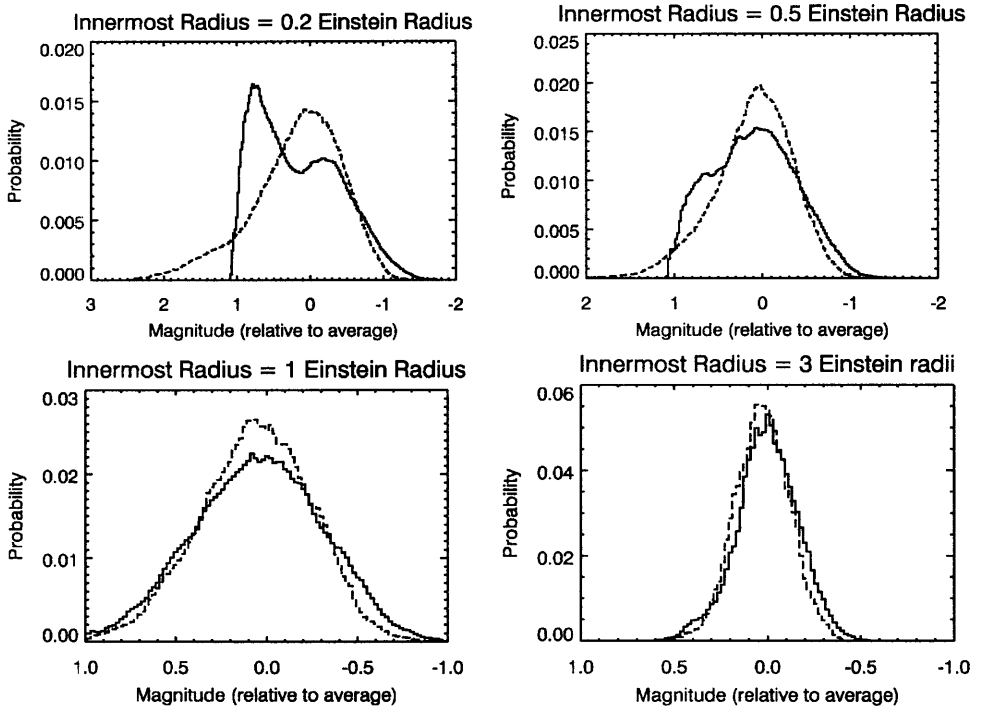

Figure 9-3: Histograms of magnitudes relative to the average for convolutions of Shakura-Sunyaev disk profiles of various sizes in the filter associated with the peak intensity at the maximum temperature T_0 ($i = 0$) with the positive parity $\kappa = 0.4$, $\gamma = 0$ magnification pattern (solid curves) and the negative parity $\kappa = \gamma = 0.6$ magnification pattern (dashed curves). The half-light radii of the disks used as sources are $0.28r_E$, $0.77r_E$, $1.58r_E$, and $4.84r_E$, respectively.

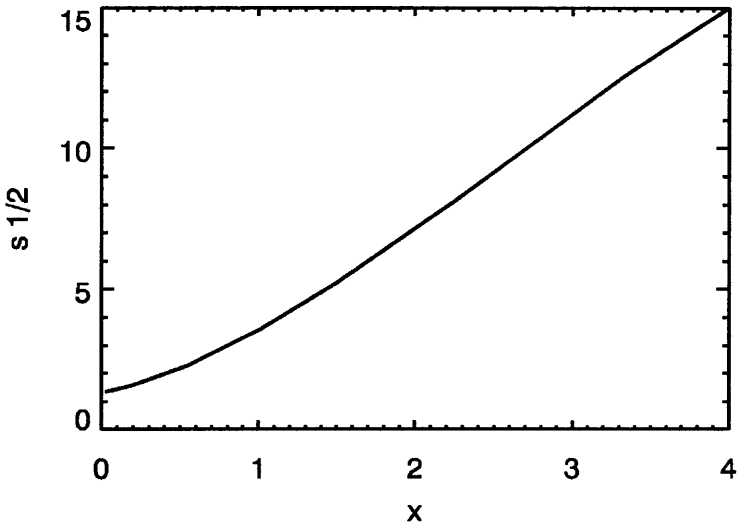

Figure 9-4: Dimensionless half-light radius ($s_{1/2} = r_{1/2}/r_{in}$) versus dimensionless wavelength, x.

is visible for the positive parity image but is absent for the negative parity image. This bump is due to the fact that an image that is a minimum (positive parity) must have at least unit magnification, so the histogram is cut off at the low-magnification end. At lower magnification, the negative parity histogram has a tail that extends down to $\Delta m \sim 2 - 3$. For the positive-parity histograms with two peaks, the left one around $\Delta m = 1$ is associated with a case where there are no extra microimage minima, while the right peak around $\Delta m = 0$ is associated with the case of one extra microimage pair (Rauch et al., 1992).

9.2 Histogram Statistics

Since the intensity from disks in different filters falls off at different rates, we can use the half-light radius, $r_{1/2}$, as an alternative measure of wavelength (see Figure 9-4). For each magnification histogram, we calculated the standard deviation or root mean square (rms) and skewness of the data and plotted these statistics against $r_{1/2}/r_E$. The results are shown in Figures 9-5 and 9-6.

For all disk sizes, the rms decreases with $r_{1/2}/r_E$. This shows that the effect of

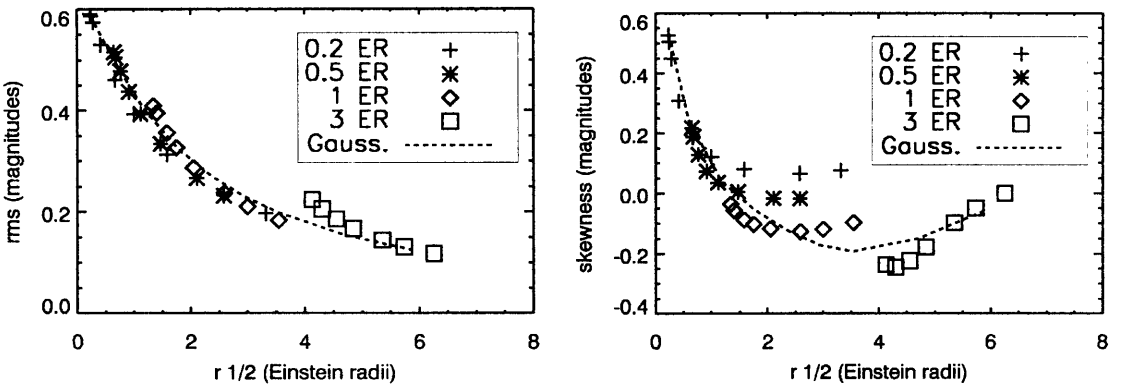

Figure 9-5: Standard deviation (rms) and skewness of convolutions of the $\kappa = 0.4$, $\gamma = 0$ magnification pattern with various Shakura-Sunyaev disk profiles. Different plot symbols are used for different values of r_{in} (given in Einstein radii). Dashed curves for the Gaussian disk models are shown for comparison. Note that positive skewness is associated with brighter (more negative) magnitudes.

microlensing is diminished at longer wavelengths and for larger disks. These trends are expected since the source must be smaller than the microlens Einstein radius for microlensing to play a significant role (see Chapter 6).

Using the same methods described in Section 9.1, we produced magnification histograms from convolutions with Gaussian disks, uniform disks, and cones. These histograms all had very similar rms and skewness as a function of $r_{1/2}$, so only the curves for the Gaussian disks are shown in Figures 9-5 and 9-6. For a given value of $r_{1/2}$, there is little practical difference between the rms values of histograms produced with the Gaussian disks and those produced with the Shakura-Sunyaev accretion disk models. This suggests that, to a good approximation, the microlensing fluctuations only depend on $r_{1/2}$, and the disk may be modeled with any reasonable surface brightness profile. We examine this claim more quantitatively in the next section.

Note that in Figure 9-4, at a given dimensionless wavelength, the half-light radius depends on r_{in} and thus on the black hole mass. Also, the scaling between the dimensionless and physical wavelengths depends on the values of r_{in} and T_0. So while the main parameter that matters in our simulations is $r_{1/2}$, for actual observations the black hole mass and disk temperature will also matter.

In the third moment of the histograms, the skewness, we begin to see some greater

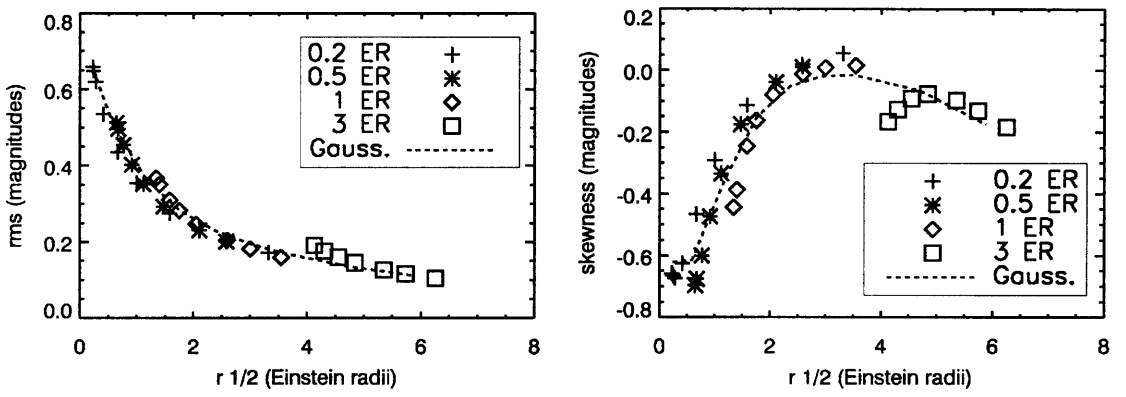

Figure 9-6: Standard deviation (rms) and skewness of convolutions of the $\kappa = 0.6$, $\gamma = 0.6$ magnification pattern with various Shakura-Sunyaev disk profiles. Different plot symbols are used for different values of r_{in} (given in Einstein radii). Dashed curves for the Gaussian disk models are shown for comparison. Note that positive skewness is associated with brighter (more negative) magnitudes.

differences between the accretion disk models and the Gaussian models. However, since the skewness is much more difficult to measure with observations than the standard deviation, these differences may well be unimportant for most applications.

9.3 Chi-square Tests

One way to compare the magnification histograms associated with different source profiles, besides looking at their rms and skewness, is to try to get a sense of the amount of observation necessary to distinguish different kinds of sources. The procedure chosen here to do this involves using chi-square tests.

First, we consider each histogram as a probability distribution for measuring different values of Δm. We then simulate a certain number of random observations (n) of each histogram, and use the results to make two new histograms, A and B (where A_k or B_k is the number of counts in bin k), each containing a sample from one of the original magnification histograms. Computing the reduced chi-square (χ^2_ν) of the two sample histograms,

$$\chi^2_\nu = \frac{1}{\nu} \sum_k \frac{(A_k - B_k)^2}{A_k + B_k}, \tag{9.2}$$

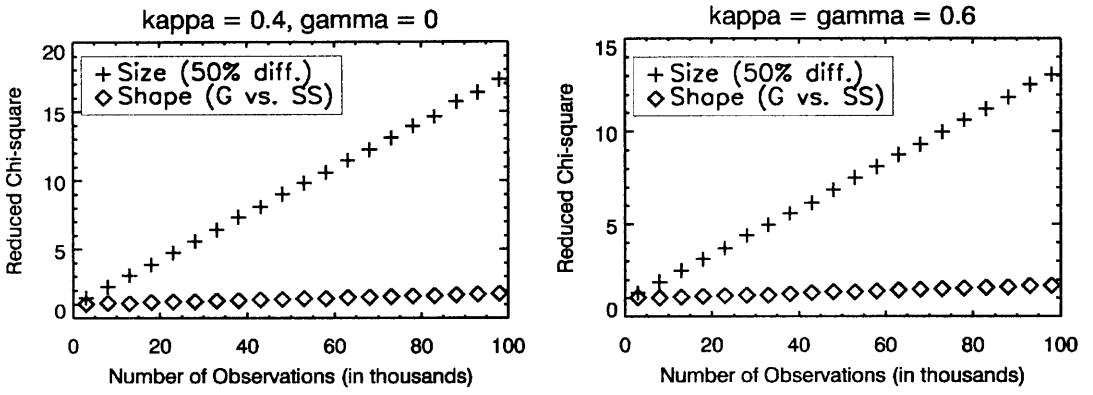

Figure 9-7: Reduced chi-square measure of the differences between histograms from convolutions with different disk models. For the shape comparison, the two models used are a Shakura-Sunyaev disk and a Gaussian disk, each with half-light radius $r_{1/2} = 0.765r_E$. The two models used for the size comparison are both Gaussian disks, one with half-light radius $r_{1/2} = 0.5r_E$ and the other with $r_{1/2} = 0.75r_E$. Higher values of χ^2_ν indicate a greater ability to distinguish the two models.

where ν is the number of degrees of freedom, gives an indication of how likely it is that the two samples came from the same parent distribution. We can use the chi-square probability function (based on the incomplete gamma function) to express the result as the probability that χ^2_ν would be greater than or equal to the value we found if the two samples were from the same parent distribution.

If we repeat these computations for various values of n, we can construct $\chi^2_\nu(n)$ and $P(n)$, the reduced chi-square and probability described above as a function of the number of observations. Since our ability to distinguish the two original histograms should increase with n, we expect that $\chi^2_\nu(n)$ should grow and $P(n)$ should fall off as we increase the number of observations. Using these functions, we can estimate a value of n that is a sufficient number of observations to tell the difference between the two cases. To decrease variability due to the random nature of this process, we create several sample distributions (for all results presented here, 10 samples) and average over the results for each value of n.

Figure 9-7 shows the reduced chi-square for representative shape and size comparisons. The slopes of $\chi^2_\nu(n)$ for comparisons between histograms of convolutions with Shakura-Sunyaev disk models and histograms of convolutions with Gaussian disks,

Table 9.1: Slopes of $\chi^2_\nu(n)$ for disk shape comparisons. The disk models listed are compared to a Shakura-Sunyaev model; all of these models have half-light radius $r_{1/2} = 0.765 r_E$. The number of observations necessary to tell that the two histograms are different with 95% confidence, $n_{95\%}$, is also listed.

Original Pattern	Disk Model	Slope of $\chi^2_\nu(n)$	$n_{95\%}$ (thousands)
$\kappa = 0.4,\ \gamma = 0$	Gaussian	$(7.834 \pm 0.163) \times 10^{-6}$	44
	Uniform	$(3.597 \pm 0.028) \times 10^{-5}$	10
	Cone	$(8.780 \pm 0.183) \times 10^{-6}$	40
$\kappa = \gamma = 0.6$	Gaussian	$(7.324 \pm 0.156) \times 10^{-6}$	52
	Uniform	$(2.813 \pm 0.022) \times 10^{-5}$	14
	Cone	$(9.396 \pm 0.175) \times 10^{-6}$	36

uniform disks, and cones are given in Table 9.1. Smaller slopes correspond to greater similarity between the models.

Note that matching the "number of observations" n to an actual number of observations to be made with a telescope is not necessarily a straightforward task. The observations in these simulations are randomly drawn from the magnification histograms. Real observations, unless separated by times greater than the characteristic time scale for microlensing fluctuations, will be correlated since the image magnitude changes smoothly over short time scales. One could multiply the number of random observations n by the characteristic time scale for the lens to estimate the total amount of time over which observations would need to be taken to determine the shape and structure of the source, but this estimate would not be very accurate since it would not account for rapid events like caustic crossings, or for periods of time much longer than the characteristic time scale over which the image magnitude stays almost constant.

One way to use the chi-square results is as a relative measure of similarity between histograms, comparing results that probe one property of the source with results that probe a different property. Table 9.2 gives the slope of $\chi^2_\nu(n)$ for comparisons between Gaussian disk models with different sizes. We can compare these results to those that examine the effect of disk shape (Table 9.1).

We can also characterize the similarity between two histograms by asking how

Table 9.2: Slopes of $\chi^2_\nu(n)$ for size comparisons between Gaussian disks. The sizes of the two disks for each chi-square test are listed in columns two and three. The number of observations necessary to tell that the two histograms are different with 95% confidence, $n_{95\%}$, is also shown here.

Original Pattern	$r_{1/2}/r_E$ #1	$r_{1/2}/r_E$ #2	Slope of $\chi^2_\nu(n)$	$n_{95\%}$ (thousands)
$\kappa = 0.4,\ \gamma = 0$	0.5	0.55	$(8.392 \pm 0.179) \times 10^{-6}$	41
	0.5	0.75	$(1.666 \pm 0.006) \times 10^{-4}$	2.4
	2.5	2.55	$(8.820 \pm 0.224) \times 10^{-6}$	48
	2.5	2.75	$(8.795 \pm 0.046) \times 10^{-5}$	3.2
$\kappa = \gamma = 0.6$	0.5	0.55	$(8.612 \pm 0.156) \times 10^{-6}$	42
	0.5	0.75	$(1.247 \pm 0.003) \times 10^{-4}$	3.8
	2.5	2.55	$(1.055 \pm 0.026) \times 10^{-5}$	51
	2.5	2.75	$(1.246 \pm 0.005) \times 10^{-4}$	4.1

many random observations we would need to be 95% confident that the parent distributions are different. The probability that the distributions are the same, as a function of the number of observations, $P(n)$, is shown in Figure 9-8 for one shape comparison and one size comparison. The results are plotted only for the positive parity image, but the negative parity case gives very similar results. The numbers of observations needed for 95% confidence ($n_{95\%}$) for all of the histogram comparisons are listed in Tables 9.1 and 9.2.

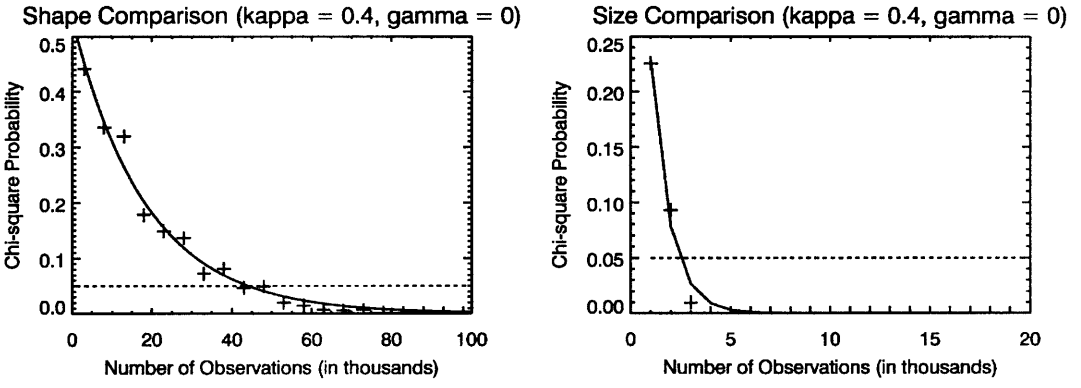

Figure 9-8: Probability that two sample distributions have the same parent distribution as a function of the number of observations in the samples. On the left we compare histograms from disks with $r_{1/2} = 0.765 r_E$ but with different shapes (a Shakura-Sunyaev model and a Gaussian model), and on the right we compare histograms from two Gaussian disks that differ in size by 50% (with half-light radii $0.5 r_E$ and $0.75 r_E$). The horizontal dashed lines show where the probability is 5%, which is the threshold we used to determine the number of observations $n_{95\%}$.

Chapter 10

Conclusions

We have produced several magnification histograms by convolving source brightness profiles with a variety of shapes and sizes with both positive and negative parity image magnification patterns. These histograms can be thought of as distributions of the probability to observe the macroimage with a certain magnification. We compared histograms associated with disks of different shapes and different sizes by computing moments of the histograms (rms and skewness), and by computing chi-square values for pairs of histograms.

By plotting rms and skewness against half-light radius (Figures 9-5 and 9-6), we discovered that for any particular disk model there is a definite dependence of rms and skewness on the half-light radius, but if we compare disk models with different shapes but the same half-light radius, the rms and skewness of the associated histograms are only slightly dependent on the shape of the model. This suggests that size differences have a more significant effect on microlensing fluctuations than shape differences do, at least for circular sources.

The chi-square tests confirm this result, showing that the number of observations needed to distinguish sources with differently-shaped brightness profiles but the same size is significantly higher than the amount needed to tell the difference between sources with different sizes but the same shape of the brightness distribution (see Figure 9-8).

One might object that in some cases, a difference in shape appears to have more

of an effect than a difference in size. For instance, by looking at Tables 9.1 and 9.2 we see that the number of observations required to distinguish a uniform disk from a Shakura-Sunyaev disk of the same size is only about one-fourth the number of observations needed to tell the difference between two Gaussian disks with half-light radii of $2.5r_E$ and $2.55r_E$. However, it is always possible to make the difference in size less significant than a difference in shape if we choose two disks with arbitrarily similar half-light radii. The problem is that we do not know if, for example, a Gaussian disk and a Shakura-Sunyaev disk with the same size are more similar to each other than two Gaussian disks that have a 10% difference in size. (Note that we are talking about the disks themselves now, not the histograms produced by convolving patterns with those disks.)

One simple way to evaluate the similarity of two disks is to look at their brightness profiles and make the judgment by eye. In Figure 10-1, we plot radial brightness distributions for a pair of disks with the same size but different shapes, and another pair with the same shape but different sizes. The slope of $\chi^2_\nu(n)$ and the number of observations needed to tell the associated histograms apart with 95% confidence for the pair of disks on the left and the pair on the right differ by less than 5%. If size and shape mattered equally to microlensing, we would therefore expect that the disks on the left were just as similar to each other as the disks on the right. However, this is clearly not the case. The disks on the left, with different shapes, have extremely different brightness distributions, whereas the brightness distributions of the disks on the right are nearly equal. Despite this observation, the chi-square tests show that it is just as difficult to tell apart the histograms associated with the disks on the left as it is those associated with the disks on the right. This is strong evidence that the dependence of microlensing variability on source shape is far weaker than the dependence on source size. We can model the accretion disk by any circular brightness profile we like—Gaussian disk, uniform disk, or any other well-behaved disk model—and our model will produce the correct results, as long as it is the correct size.

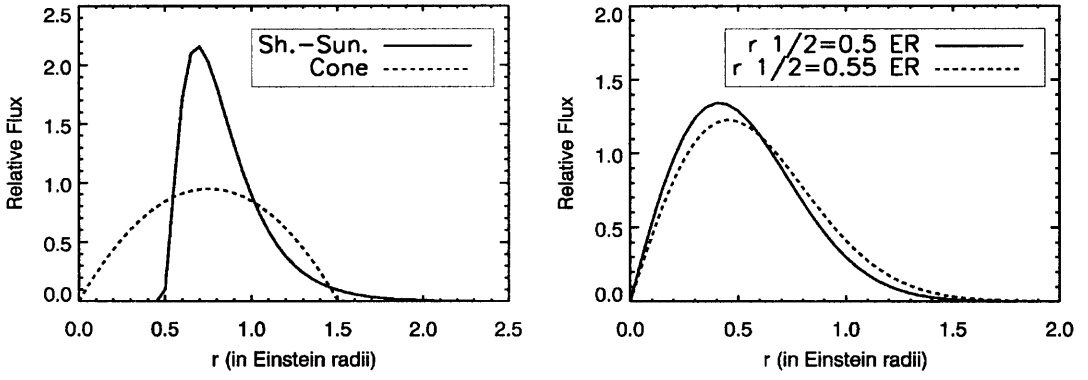

Figure 10-1: Disk profiles for disks with different shapes (left) and sizes (right). The disks on the left both have half-light radius $r_{1/2} = 0.765 r_E$, but one is a Shakura-Sunyaev disk (solid line) and the other is a cone (dashed line). The disks on the right are both Gaussian disks, but they have slightly different half-light radii as indicated in the legend. The slope of $\chi^2_\nu(n)$ is about the same for the histograms that come from each pair of disks, even though the disks on the right are much more similar to each other than those on the left.

Appendix A

Elliptical Disk Models

The results of the previous few chapters only used accretion disk models with circular symmetry. In actual observations, however, even if a disk is circular it is likely to be inclined at some angle relative to our line of sight, so that the projection of the disk on the sky looks more like an ellipse. We can ask, then, what kind of microlensing fluctuations we get with various elliptical sources.

It is safe to assume that elliptical models with the same shape but different sizes will lead to magnification histograms that vary with size in a similar manner to the circular models, so we will not examine the effect of the overall disk size here. The properties of the elliptical disks that we are interested in are their ellipticity and their orientation. To study these properties, we use elliptical Gaussians for the disk model. We can write these models as

$$G_{ell}(x,y) = \frac{L}{2\pi ab} e^{-\frac{\xi^2}{2a^2} - \frac{\zeta^2}{2b^2}}, \tag{A.1}$$

where L is the total disk luminosity, $\xi = x\cos\theta - y\sin\alpha$, $\zeta = x\sin\theta + y\cos\alpha$, and the x and y directions line up with the rows and columns of our two-dimensional array. This model has three parameters: a and b, the widths in the x and y directions before rotation; and α, the angle of rotation (measured clockwise from the positive y-axis).

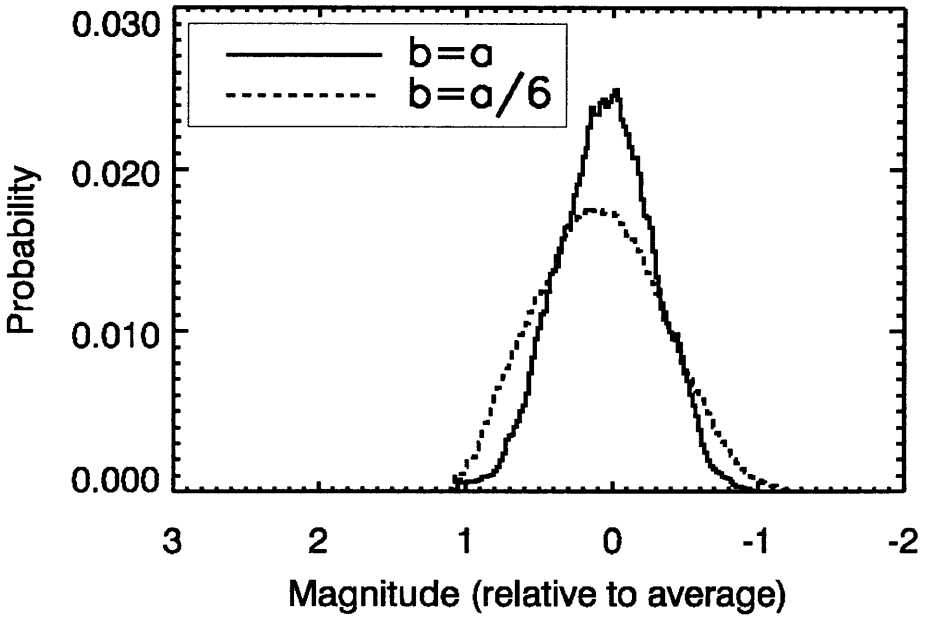

Figure A-1: Magnification histograms for convolutions of the $\kappa = 0.4$, $\gamma = 0$ pattern with a circular Gaussian (solid line), and with an elliptical Gaussian whose major axis is 6 times longer than its minor axis (dashed line).

A.1 Ellipticity

In the first set of models, a and α remain fixed while b varies from $b = a$ to $b = a/6$. We convolved these models with the positive parity $\kappa = 0.4$, $\gamma = 0$ magnification pattern. Two of the resulting magnification histograms are shown in Figure A-1.

Results of chi-square tests between the circular model ($b = a$) and models with various ellipticities are listed in Table A.1. The slopes are quite large compared to those in Chapter 9. However, in some sense a change in ellipticity is more of a change in size (but only in one dimension) than a change in the shape of the brightness distribution.

A.2 Orientation

In the second set of models, a and b remain fixed (with $a = 4b$) and α varies from 0° to 90°. Convolving these models with the $\kappa = 0.4$, $\gamma = 0$ magnification pattern would

Table A.1: Slopes of $\chi^2_\nu(n)$ for elliptical Gaussians with different ellipticities. The disk models listed are compared to a circular Gaussian model, and a/b is the ratio of the width along the major axis to the width along the minor axis. The number of observations necessary to tell that the two histograms are different with 95% confidence, $n_{95\%}$, is also given.

a/b	Slope of $\chi^2_\nu(n)$	$n_{95\%}$ (thousands)
1.5	$(1.450 \pm 0.005) \times 10^{-4}$	3.6
3	$(5.167 \pm 0.009) \times 10^{-4}$	< 2
6	$(7.610 \pm 0.012) \times 10^{-4}$	< 2

Table A.2: Slopes of $\chi^2_\nu(n)$ for elliptical Gaussians oriented at different angles with respect to the shear of the $\kappa = \gamma = 0.6$ magnification pattern. One disk in each case has its major axis aligned with the shear, and the angle between the major axis of the other disk and the shear is given in the first column. The number of observations necessary to tell that the two histograms are different with 95% confidence, $n_{95\%}$, is also given.

Angle	Slope of $\chi^2_\nu(n)$	$n_{95\%}$ (thousands)
30°	$(8.285 \pm 0.034) \times 10^{-5}$	4.0
60°	$(3.885 \pm 0.007) \times 10^{-4}$	< 2
90°	$(5.249 \pm 0.007) \times 10^{-4}$	< 2

not tell us much since that pattern has no preferred direction. The negative parity $\kappa = \gamma = 0.6$ pattern has shear in the x-direction, so we convolve the models with that pattern and examine how the magnitude fluctuations vary as the angle between α and the direction of shear changes. Two of the resulting magnifiction histograms are shown in Figure A-2.

Results of chi-square tests between the parallel model ($\alpha = 0°$) and models with various orientations are listed in Table A.2.

A.3 Conclusions

In both cases, when we vary ellipticity and when we vary orientation, the slopes of $\chi^2_\nu(n)$ are generally higher and the values of $n_{95\%}$ are generally lower than for the shape comparisons and the size comparisons of Chapter 9. This suggests that,

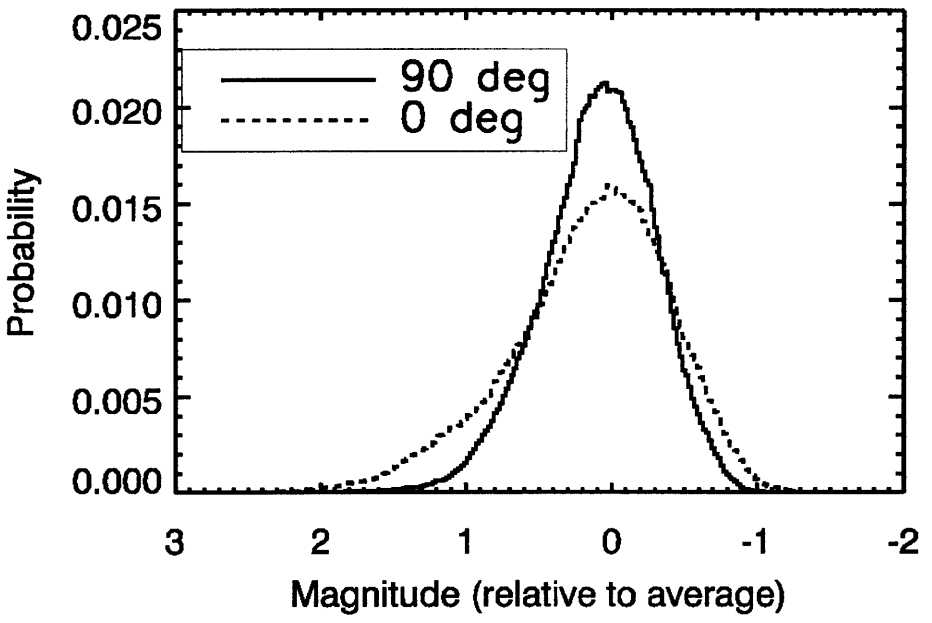

Figure A-2: Magnification histograms for convolutions of the $\kappa = \gamma = 0.6$ pattern with elliptical Gaussians, one oriented parallel to the shear (solid line), and the other perpendicular (dashed line).

unlike the shape of the brightness distribution for circular disk models, ellipticity and orientation can have quite a large effect on microlensing fluctuations. Further investigations of non-circular disk models may therefore prove interesting.

Bibliography

Agol, E., & Krolik, J. 1999, ApJ, **524**, 49

Alard, C. 1995, in IAU Symp. 173, Astrophysical Applications of Gravitational Lensing, ed. C. S. Kochanek & J. N. Hewitt (Boston: Kluwer)

Alcock, C., Akerlof, C. W., Allsman, R. A. et al. 1993, Nature, **365**, 621

Aubourg, E., Bareyre, P., Bréhin, P. et al. 1993, Nature, **365**, 623

Bond, I. A., Udalski, A., Jaroszyński, M. et al. 2004, preprint, astro-ph/0404309

Burud, I., Courbin, F., Magain, P., Lidman, C., Hutsemékers, D., Kneib, J.-P., Hjorth, J., Brewer, J., Pompei, E., Germany, L., Pritchard, J., Jaunsen, A. O., Letawe, G., & Meylan, G. 2002, A&A , **383**, 71

Carroll, S. 2004, An Introduction to General Relativity: Spacetime and Geometry (Boston: Addison Wesley)

Chae, K.-H. 2003, MNRAS, **346**, 746

Chartas, G., Eracleous, M., Agol, E., & Gallagher, S. C. 2004, preprint, astro-ph/0401240

Chiba, M. 2002, ApJ, **565**, 17

Chwolson, O. 1924, Astron. Nachr., **221**, 329

Courbin, F., Magain, P., Keeton, C. R., Kochanek, C. S., Vanderriest, C., Jaunsen, A. O., & Hjorth, J. 1997, A&A, **324**, L1

Courbin, F., Saha, P., & Schechter, P. 2002 in Gravitational Lensing: An Astrophysical Tool, ed. F. Courbin & D. Minniti (Berlin:Springer), 1

Dalal, N., & Kochanek, C. S. 2002, ApJ, **572**, 25

Dyson, F. W., Eddington, A. S., & Davidson, C. R. 1920, Mem. R. Astron. Soc., **62**, 291

Eddington, A. S. 1920, Space, Time, and Gravitation (Cambridge: Cambridge Univ. Press)

Einstein, A. 1936, Science, **84**, 506

Evans, N. W., & Witt, H. J. 2003, MNRAS, **345**, 1351

Falco, E. E., Wambsganss, J., & Schneider, P. 1991, MNRAS, **251**, 698

Fort, B., Prieur, J. L., Mathez, G., Mellier, Y., & Soucail, G. 1988, A&A, **200**, L17

Gaudi, B. S., & Petters, A. O. 2002, ApJ, **574**, 970

Gould, A., & Loeb, A. 1992, ApJ, **396**, 104

Gould, A., & Miralda-Escudé, J. 1997, ApJ, **483**, L13

Hewitt, J. N., Turner, E. L., Lawrence, C. R., Schneider, D. P., Gunn, J. E. et al. 1987, ApJ, **321**, 706

Inada, N., Becker, R. H., Burles, S. et al. 2003, AJ, **126**, 666

Irwin, M. J., Webster, R. L., Hewett, P. C., Corrigan, R. T., & Jedrzejewski, R. I . 1989, AJ, **98**, 1989

Iwamuro, F., Motohara, K., Maihara, T. et al. 2000, PASJ, **52**, 25

Jaroszyński, M., Wambsganss, J., & Paczyński, B. 1992, ApJ, **396**, L65

Kayser, R., Refsdal, S., & Stabell, R. 1986, A&A, **166**, 36

Keeton, C. R., Gaudi, B. S., & Petters, A. O. 2003, ApJ, **598**, 138

Kochanek, C. S. 2004, ApJ, **605**, 58

Kochanek, C. S., & Schechter, P. L. 2004, in Measuring and Modeling the Universe, from the Carnegie Observatories Centennial Symposia, ed. W.L. Freedman (Cambridge: Cambridge Univ. Press), 117

Kochanek, C. S., Falco, E. E., Impey, C., Lehar, J., McLeod, B., & Rix, H.-W., CASTLES Survey Website, http://cfa-www.harvard.edu/castles/

Koopmans, L. V. E., Treu, T., Fassnacht, C. D., Blandford, R. D., & Surpi, G. 2003, ApJ, **599**, 70

Kristian, J., Groth, E. J., Shaya, E. J., Schneider, D. P., Holtzman, J. A., Baum, W. A., Campbell, B., Code, A., Currie, D. G., Danielson, G. E., Ewald, S. P., Hester, J. J., Light, R. M., Lynds, C. R., O'Neil, E. J., Jr., Seidelmann, P. K., Westphal, J. A. 1993, AJ, **106**, 1330

Lewis, G. F., & Ibata, R. A. 1998, ApJ, **501**, 478

Lopes, A., & Miller, L. 2004, MNRAS, **348**, 519

Lynds, R., & Petrosian, V. 1986, BAAS, **18**, 1014

Mao, S., & Paczyński, B. 1991, ApJ, **374**, L37

Mao, S., Jing, Y., Ostriker, J. P., & Weller, J. 2004, ApJ, **604**, L5

Metcalf, R. B., & Madau, P. 2001, ApJ, **563**, 9

Metcalf, R. B., Moustakas, L. A., Bunker, A. J., & Parry, I. R. 2003, preprint, astro-ph/0309738

Moore, B., Ghigna, S., Governato, F., Lake, G., Quinn, T., Stadel, J., & Tozzi, P. 1999, ApJ, **524**, L19

Moustakas, L. A., & Metcalf, R. B. 2003, MNRAS, **339**, 607

Narayan, R., & Bartelmann, M. 1996, in Formation of Structure in the Universe, ed. A. Dekel & J. P. Ostriker, (Cambridge: Cambridge Univ. Press); preprint, astro-ph/9606001

Ostensen, R., Refsdal, S., Stabell, R., Teuber, J., Emanuelsen, P. I. et al. 1996, A&A, **309**, 59

Paczyński, B. 1986a, ApJ, **301**, 503

Paczyński, B. 1986b, ApJ, **304**, 1

Press, W. H., Teukolsky, S. A., Vetterling, W. T., & Flannery, B. P. 1992, Numerical Recipes in C, 2nd ed., (Cambridge: Cambridge University Press)

Rauch, K. P., & Blandford, R. D. 1991, ApJ, **381**, L39

Rauch, K. P., Mao, S., Wambsganss, J., & Paczyński, B. 1992, ApJ, **386**, 30

Refsdal, S. 1964, MNRAS, **128**, 307

Refsdal, S., & Stabell, R. 1993, A&A, **278**, L5

Reimers, D., Hagen, H.-J., Baade, R., Lopez, S., & Tytler, D. 2002, A&A, **382**, L26

Schechter, P. L., & Moore, C. B. 1993, AJ, **105**, 1

Schechter, P. L., Gregg, M. D., Becker, R. H., Helfand, D. J., & White, R. L. 1998, AJ, **115**, 1371

Schechter, P. L., & Wambsganss, J. 2002, ApJ, **580**, 685

Schechter, P. L. 2003, in Gravitational Lensing: A Unique Tool for Cosmology, ed. D. Valls-Gabaud & J.-P. Kneib, (ASP Conference Series)

Schechter, P. L., Udalski, A., Szymański, M., Kubiak, M., Pietrzyński, G., Soszyński, I., Woźniak, P., Zebruń, K., Szewczyk, O., & Wyrzykowski, L. 2003, ApJ, **584**, 657

Schechter, P. L., Wambsganss, J., & Lewis, G. F. 2004, preprint, astro-ph/0403558

Schneider, P., & Weiss, A. 1987, A&A, **171**, 49

Seljak, U., & Hirata, C. M. 2004, Phys. Rev. D, **69**, 043005

Shakura, N. I., & Sunyaev, R. A. 1973, A&A, **24**, 337

Shalyapin, V. N., Goicoechea, L. J., Alcalde, D., Mediavilla, E., Muñoz, J. A., & Gil-Merino, R. 2002, ApJ, **579**, 127

Shapiro, I. I. 1964, Phys. Rev. Lett., **13**, 789

Soucail, G., Fort, B., Mellier, Y., Picat, J. P. 1987a, A&A, **172**, L14

Soucail, G., Mellier, Y., Fort, B., Hammer, F., Mathez, G. 1987b, A&A, **184**, L7

Treyer, M., & Wambsganss, J. 2004, A&A, **416**, 19

Tyson, J. A. 1988, AJ, **96**, 1

Tyson, J. A., Valdes, F., & Wenk, R. A. 1990, ApJ, **349**, L1

Udalski, A., Szymański, M., Kaluzny, J., Kubiak, M., Mateo, M. 1992, Acta Astron., **42**, 253

Udalski, A., Szymański, M., Kaluzny, J., Kubiak, M., Krzemiński, W. et al. 1993, Acta Astron., **43**, 289

Vanderriest, C., Wlerick, G., Lelievre, G., Schneider, J., Sol, H., Horville, D., Renard, L., & Servan, B. 1986, A&A, **158**, L5

Walsh, D., Carswell, R. F., & Weymann, R. J. 1979, Nature, **279**, 381

Wambsganss, J. 1990, Ph.D. thesis, Ludwig-Maximilians-Universität, München, available as MPA550, Max-Planck-Institut für Astrophysik

Wambsganss, J., Paczyński, B., & Katz, N. 1990, ApJ, **352**, 407

Wambsganss, J., Schneider, P., & Paczyński, B. 1990, ApJ, **358**, L33

Wambsganss, J., Paczyński, B. 1991, AJ, **102**, 864

Wambsganss, J. 1992, ApJ, **386**, 19

Wambsganss, J., Bode, P., & Ostriker, J. P. 2004, ApJ, **606**, L93

Weymann, R. J., Latham, D., Angel, J. R. P., Green, R. F., Liebert, J. W., Turnshek, D. E., & Tyson, J. A. 1980, Nature, **285**, 641

Wisotzki, L., Koehler, T., Kayser, R., & Reimers, D. 1993, A&A, **278**, L15

Wisotzki, L., Becker, T., Christensen, L., Helms, A., Jahnke, K., Kelz, A., Roth, M. M., & Sanchez, S. F. 2003, A&A, **408**, 455

Witt, H. J., Mao, S., & Schechter, P. L. 1995, ApJ, **443**, 18

Woźniak, P. R., Alard, C., Udalski, A., Szymański, M., Kubiak, M., Pietrzyński, G., Zebruń, K. 2000a, ApJ, **529**, 88

Woźniak, P. R., Udalski, A., Szymański, M., Kubiak, M., Pietrzyński, G., Soszyński, I., & Zebruń, K. 2000b, ApJ, **540**, L65

Wyithe, J. S. B., Webster, R. L., & Turner, E. L. 2000, MNRAS, **318**, 762

Wyithe, J. S. B., Webster, R. L., Turner, E. L., & Agol, E. 2000, MNRAS, **318**, 1105

Wyithe, J. S. B., Agol, E., & Fluke, C. J. 2002, MNRAS, **331**, 1041

Yonehara, A. 2001, ApJ, **548**, L127

Zwicky, F. 1937a, Phys. Rev. Lett., **51**, 290

Zwicky, F. 1937b, Phys. Reb. Lett., **51**, 679